RÉPUBLIQUE DE CÔTE D'IVOIRE

UNION - DISCIPLINE - TRAVAIL

MINISTERE DE L'ENSEIGNEMENT SUPERIEUR ET DE LA RECHERCHE SCIENTIFIQUE

Université Félix Houphouët-Boigny

UNITE DE FORMATION ET DE RECHERCHE SCIENCES DES STRUCTURES DE LA MATIERE ET DE TECHNOLOGIE

THEORY AND COMPUTATION OF ENERGY MATERIALS

Physical Modeling and Diagnostics

SPONSORED BY THE

Federal Ministry of Education and Research

N°: 831

INTERNATIONAL MASTER PROGRAM

IN RENEWABLE ENERGY AND GREEN HYDROGEN

SPECIALITY: GREEN HYDROGEN PRODUCTION and TECHNOLOGY

MASTER THESIS

Topic:

Comparative Analysis of Pore Network Modelling (PNM) and Computational Fluid Dynamics (CFD) for Transport Modeling in Alkaline Water Electrolyser Porous Electrode

Presented on 24/09/2025 and by:

Traore Mariam

Jury:

Dr (MC) ZAHIRI Eric Pascal	**President**
Dr KOUADIO Kouakou	**Examiner**
Dr TOUALY Elisée	**Major Supervisor**
Prof. Dr. Nat. Michael Eikerling	**Co-Supervisor**
Dr. Thomas Kadyk	**Co-Supervisor**

Academic year: 2024-2025

Foreword and acknowledgements

This work has been made possible through the support of several institutions and individuals, to whom I would like to express my sincere gratitude.

First of all, I sincerely thank the **German Federal Ministry of Education and Research (BMBF)** and the **WASCAL program** for awarding me the scholarship that enabled me to pursue this International Master's degree in Energy and Green Hydrogen.

I would also like to express my sincere to the President of Félix Houphouët-Boigny University (Côte d'Ivoire)**, Prof. Zie BALLO** for the opportunity to study during the third semester, and for the honor of awarding me the certificate. My gratitude also goes to all the academic and administrative staff of Félix Houphouët-Boigny University**.**

I warmly thank the Director, **Prof. Kouassi Edouard**, the Deputy Director **Prof.N'golo Koné**, the Coordinator of the H2 Programme, **Dr. Wanignon Ferdinand Fassinou**, and the Scientific Coordinator, **Prof. Fatoma Soro**, of the graduate school program (GSP) of Côte d'Ivoire, for their academic and administrative guidance throughout my studies.

I also extend my sincere thanks to the President of the University of Lomé, **Prof. Adama Mawule Kpodar**, for his support during the first semester, and to the President of Abdou Moumouni University (Niger), **Prof. Mamadou Saidou**, for his academic guidance and support during the second semester. As well as the director of the graduate school program (GSP) of Niger, **Prof. Rabbani Adamou** at and Abdou Moumouni University and the director of the graduate school program (GSP) of Lomé, **Prof Agboka Komi.**

My profound gratitude goes to my supervisor, **Prof. Dr. rer. nat. Michael Eikerling**, Director of the Theory and Computation of Energy Materials Institute (IET-3) at Forschungszentrum Jülich, Germany for the warm welcome, support, and resources provided during my internship period, as well as for his invaluable advice, constant availability, and rigorous scientific guidance.

I am deeply grateful to my other supervisors **Dr. Thomas Kadyk, Dr. Elisée Toualy, and Steffen Hess**, for their valuable guidance, constructive suggestions, and continuous encouragement throughout this

work. Their complementary expertise, constant availability, and genuine commitment to my progress have been a great source of motivation. I owe them a great deal for the knowledge I have gained, the scientific rigor I have developed, and the confidence they have inspired in me. Their guidance has truly and profoundly enriched this thesis.

I also wish to acknowledge the **jury members**, **Dr. (MC) Eric Pascal Zahiri**, for the honor of serving as President of the jury, and **Dr. Kouakou Kouadio**, for kindly accepting to examine this work.

I also wish to thank the **team members from Togo and Niger**, with whom I shared the first and second semesters, for their collaboration and solidarity.

I am equally thankful to all the **lecturers and researchers involved in the WASCAL programme**, for their dedication to training the next generation of African scientists.

Finally, I would like to thank my **family, friends, and classmates** for their moral and material support, and for their constant encouragement, without which this work would not have been possible.

Abstract

Green hydrogen production via alkaline water electrolysis (A-WE) is a crucial technology for sustainable energy transition. The efficiency and durability of electrolyzers strongly depend on the transport properties within porous electrodes. This thesis presents a comparative analysis of two numerical modelling approaches, Pore Network Modeling (PNM) and Computational Fluid Dynamics (CFD), to predict transport phenomena in realistic 3D microstructures of sintered nickel electrodes obtained from X-ray microtomography (µCT).

Microtomography µCT image was processed and SNOW2 algorithm was used to extract detailed pore networks. The porosity and interfacial area per volume were computed. These geometric properties were validated against image analysis data with agreement, confirming the accuracy of the reconstruction method. Subsequently, single-phase flow simulations were conducted using the pore network (PN) (OpenPNM) with various geometric models and CFD (OpenFOAM) directly on meshed µCT data to evaluate absolute permeability and tortuosity.

Results demonstrated a strong correlation between PNM and CFD for tortuosity prediction, with 1.4% relative error, highlighting PNM's ability to reliably represent the complexity of diffusion pathways. Permeability predictions showed larger variations depending on pore and throat geometry, with relative errors ranging from 17% (cones and cylinders) to 260% (cubes and cuboids). PNM simulations was performed in 15 minutes while CFD simulation took around 7 hours. These results show PNM computational efficiency and its flexibility to simulate multiple geometric configurations rapidly, enabling comprehensive parametric studies and optimization of porous media microstructures. This capability supports accelerated design of porous layers with enhanced transport properties, potentially improving electrolyzer performance and lifespan while reducing experimental costs.

So, validated by CFD or experimental data, PNM proves to be an effective tool for predicting transport phenomena in porous electrodes. Its ability to efficiently explore diverse pore geometries makes it invaluable for guiding rational design and innovation in alkaline water electrolysis technology and other electrochemical applications.

Keywords: Alkaline Water Electrolysis; Pore Network Modeling; Computational Fluid Dynamics; Permeability; Tortuosity.

Résume

La production d'hydrogène vert par électrolyse de l'eau à travers l'électrolyseur alcalin est une technologie clé pour la transition énergétique durable. L'efficacité et la durabilité des électrolyseurs dépendent de manière significative des propriétés de transport au sein des électrodes poreuses. Ce mémoire présente une analyse comparative entre deux approches numériques, la modélisation par réseau de pores (PNM) et la dynamique des fluides numérique (CFD), pour prédire les phénomènes de transport dans la microstructure 3D réaliste de nickel fritté obtenue par microtomographie X (µCT).

L'image µCT a été traitée pour obtenir une image binaire distincte des phases solide et poreuse. Ensuite, l'algorithme SNOW2 a été appliqué sur cette image traitée afin d'extraire le réseau poreux. Les propriétés géométriques telles que la porosité et la surface interfaciale par volume ont été calculées et validées par comparaison avec les données d'analyse d'image, montrant un excellent accord et confirmant ainsi la précision de la méthode d'extraction du réseau. Des simulations d'écoulement monophasique ont été réalisées avec PNM (OpenPNM) pour plusieurs modèles géométriques et avec CFD (OpenFOAM) sur maillages issus de µCT afin d'évaluer la perméabilité et la tortuosité.

Les résultats montrent une très bonne corrélation entre PNM et CFD pour la tortuosité, avec un écart relatif de 1,4 %, attestant la capacité de PNM à représenter la complexité des chemins de diffusion. La perméabilité, quant à elle, varie selon la géométrie des pores, avec des erreurs relatives comprises entre 17% (cônes et cylindres) à 260 % (cubes et parallélépipèdes). Les simulations PNM ont été effectuées en 15 min tandis que celles de CFD ont pris environ 7 heures. Ces résultats montrent la force de PNM dans sa rapidité et sa polyvalence pour tester rapidement divers types de géométries, ce qui favorise les études paramétriques et l'optimisation des microstructures des milieux poreux. Cette capacité répond aux besoins croissants de conception rapide de couches poreuses aux propriétés de transport améliorées, pour une meilleure performance et une durée de vie des électrolyseurs tout en réduisant les coûts expérimentaux.

Par conséquent, PNM, validée par CFD ou par des données expérimentales, apparaît comme un outil performant pour la prédiction des phénomènes de transport dans les électrodes poreuses. Sa flexibilité à modéliser diverses architectures poreuses en fait une méthode stratégique pour soutenir la conception rationnelle et l'innovation dans les technologies d'électrolyse alcaline et au-delà.

Mots-clés : Électrolyse Alcaline ; Modélisation par Réseau de Pores ; Dynamique des Fluides Numérique ; Perméabilité ; Tortuosité.

Acronyms and abbreviations

- **A-WE**: Alkaline Water Electrolyser
- **CFD**: Computational Fluid Dynamics
- **CPU**: Central Processing Unit
- **DNS**: Direct Numerical Simulation
- **EDT**: Euclidean Distance Transform
- **FVM:** Finite Volume Method
- **GSP**: Graduate Studies Programm
- **µCT**: Microtomography
- **PBI**: Polybenzimidazole
- **PDEs**: Partial Differential Equations
- **PNM**: Pore Network Modeling
- **PPS**: Polyphenylene Sulfide
- **SNOW**: Sub-Network of Over-segmented Watershed
- **VP-DVB**: Vinylpyridine-Divinylbenzene

List of tables

List of figures

TABLE OF CONTENTS

General introduction

The energy transition is one of today's greatest challenges in tackling climate change and reducing reliance on fossil fuels. Achieving it demands a substantial expansion of renewable sources like solar and wind. Yet, because these resources are intermittent, effective energy storage solutions are essential (De Sá, 2024; Misaghian 2022). Green hydrogen, produced by water electrolysis using electricity from renewable energy is emerging as a key energy carrier for large-scale storage and decarbonization of various sectors. Unlike fossil fuels, green hydrogen only produces water and energy without releasing harmful carbon emissions. Hydrogen plays a crucial role both as an energy storage medium and as a chemical feedstock, making it indispensable for sectors such as clean mobility, industrial processes, and power generation (Davey, 2024).

The Green hydrogen technology has been recognized as one of the most promising technological pathways for large-scale and efficient conversion of renewable electricity to chemical energy, contributing to the establishment of a carbon-free energy society. A way to produce clean hydrogen is by using electrolysis, this is splitting water into oxygen and hydrogen as shown on Figure1.

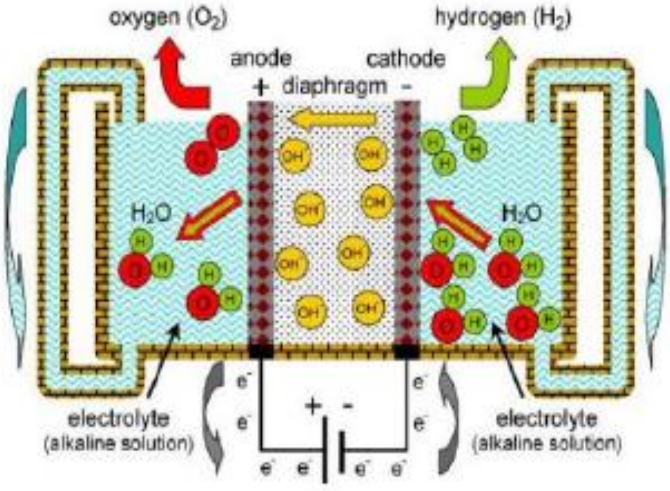

Figure 1: Alkaline water electrolysis

Electrolyzer consists of various components, such as current collectors, flow distributors, membranes or diaphragms and porous electrodes. A particular emphasis in this work is placed on the porous electrodes in the specific context of alkaline electrolysis cells.

Electrodes are conductive surfaces where electrochemical reactions occur. They allow electric current to pass through the electrolyte, enabling the conversion of water into hydrogen and oxygen gases. Their microstructure, by the porosity, the distribution of pore sizes, and the spatial connectivity of pore space, directly affects mass, heat and charge transport phenomena, and thus influences the electrochemical cell's efficiency and performance (Yang et al., 2020). Understanding the interplay between all of the mentioned transport phenomena is of great importance to create working and efficient electrolyzers. However, their intrinsic complexity makes understanding the transport mechanisms particularly challenging. One way to get insight into the properties and characteristics is to conduct various experiments, like porosimetry. In general, these experiments are time-consuming and expensive. Therefore using numerical approach appears as a valuable way and are widely applied.

A common method used to simulate the behavior of the flow through porous media is Computational Fluid Dynamics (CFD). Image data for the porous structures gained from computed tomography is converted into a mesh and the flow can be simulated . However, the computational effort of these kinds of simulations is high, especially for a multi-phase flow regime, so alternative approaches are investigated in this work. Many studies have shown that Pore Network Modelling (PNM) can be used to simulate the flow through the porous media and can be used as an alternative approach (Huang et al. 2020; Eghbalmanesh et al., 2024). Unlike CFD, Pore Network Modelling (PNM) uses a simplified pore network (PN) to simulate the two-phase flow. The fundamental idea behind Pore Network Models (PNMs) is to represent the pore space as a discrete network composed of individual pores connected by narrow channels called throats. Simulations are then performed on this simplified network using transport algorithms to study fluid flow. In addition to speed and simplicity, PNMs have some advantages over the more widely used macro-homogenous models. PNMs can resolve realistic saturation profiles and have a direct connection between the structure and topology of the porous material and the transport processes (Gostick et al. 2016; Huang et al., 2020). Comparing PNM and CFD can help to determine which modelling method best represents the transport properties in a porous material, while balancing accuracy, computational cost and applicability.

The objective of this work is thus to perform a comparative analysis of pore network and computational fluid dynamics approaches for transport modeling in porous materials. This study focuses on realistic 3D microstructures of sintered nickel, used as electrode material in alkaline water electrolyzers, which are obtained via X-ray microtomography (µCT). By leveraging µCT data, the aim is to predict key transport properties critical to electrolyzer performance, such as absolute permeability, and tortuosity. This comparison seeks to assess the accuracy, computational efficiency, and practical applicability of PNM modelling approch for optimizing porous media design and enhancing electrochemical device efficiency. The analysis and reconstruction of the grey-scaled image stacks resulting from the CT is important for the following simulations, both, for PNM and CFD. This work is structured as follows, chapter one presents the literature review. Chapter two focuses on the materials and methodology used to conduct this work. The methodology used is presented as follow:

The first step will focus on reconstructing the pore network from X-ray microtomography (µCT) images using SNOW2 extraction methods. The resulting geometrical properties computed, porosity and interfacial surface area will then be compared with available image analysis data for extraction method validation in the second step. Subsequently, in the third step, simulations will be performed with PNM and CFD to compute transport properties (permeability and turtuosity). The simulations results will be compared between the two approaches to evaluate the consistency, strengths, and limitations of PNM approaches. For the PNM the open-source package OpenPNM and for the CFD the open-source libraries of OpenFOAM are used. The following steps summarize the work done in this thesis.

- Extract pore networks from µCT image of sintered nickel using snow2 method available in OpenPNM.
- Comparing the extracted network's geometrical properties with image analysis data.
- To perform transport simulations and compare simulation results obtained from PNM with those from CFD to evaluate PNM modeling accuracy, benefits, and limitations.

Chapter 3 will then present the results of those different steps followed by the main conclusion.

Chapter 1:

Literature review

Introduction

This chapter provides a concise background to set the context for our study on alkaline water electrolysis (A-WE). We then review the current state of research on the technology, focusing on its main components, electrodes, and membranes.

1.1. Alkaline water electrolysis

Alkaline water electrolysis (A-WE) accounts for 60 % of the installed capacity of electrolyzers worldwide, and three-quarters of manufacturing capacity today is for alkaline electrolysers. It has been widely utilized since the beginning of the 20th century. Much knowledge about this technology has been acquired since the 1920s. There are different reasons why alkaline electrolysis is playing a major role in 2025 as the most used technology for electrolysis (Russo, 2024):

1. Mature technology: Reliable and widely used technology, with many industries working on it, such as Thyssenkrupp and Green Hydrogen System (Campo Schneider *et al.*, 2024).

2. Cost-wise: It costs less than other methods, especially for large-scale hydrogen production, due to the usage of platinum group metal-free electrodes and the avoidance of expensive ion-exchange membranes

3. Long-term operation: Even with harsh alkaline operational conditions, it is stable for long-term, continuous, and intermittent use.

4. Scalable: Alkaline systems can produce large amounts of hydrogen in large plant projects, which is necessary to meet the high demand for hydrogen that is required today.

In Figure 2, a schematic overview of a typical alkaline water electrolyzer is shown.

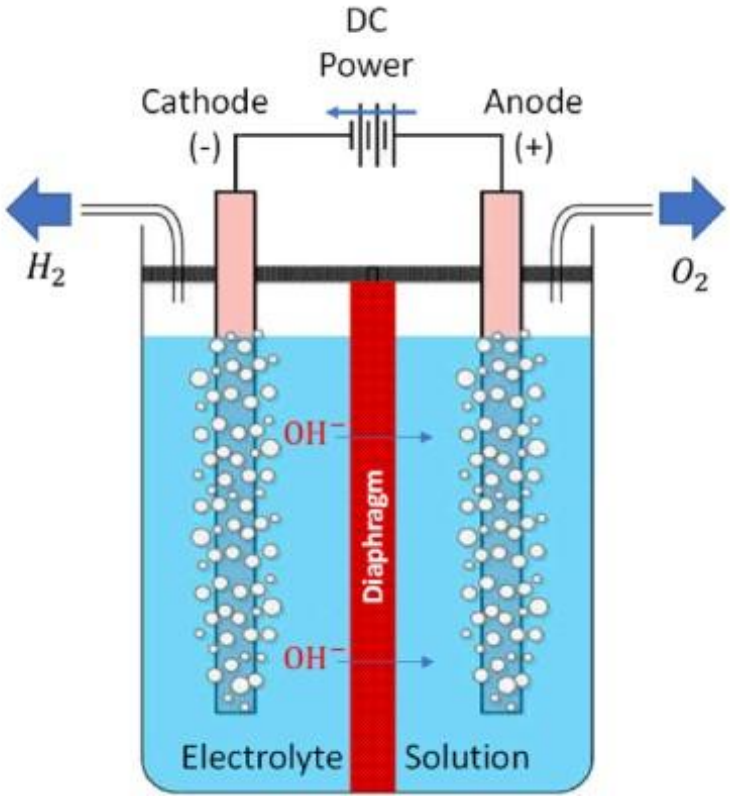

Figure 2: Schematic of an alkaline water electrolyzer

1.2. A-WE Cell components

An alkaline electrolyzer cell consists of two electrodes (an anode and a cathode) separated by a diaphragm and immersed in a liquid electrolyte, typically a highly concentrated solution of potassium hydroxide (KOH) or sodium hydroxide (NaOH) solution. Those two types of electrolytes operate with hydroxide ions, resulting in a pH of 13–14. One of a critical part of an alkaline electrolyzer is the separator. Asbestos diaphragms, which are porous, were used for a long time until they were banned in the mid-1970s due to health risks. Various membrane substitutes have since been introduced, including

IMET® (Russo 2024) inorganic ion exchange membranes. The diaphragm generally consists of a porous zirconium oxide ceramic deposited on an open mesh polyphenylene sulfide fabric (Agfa's Zirfons, 500 mm thick) (Riaz et al. 2025). As for the electrodes, they are made of nickel and stainless steel and/or potentially metallic alloys based on transition metal compounds, such as Ni, Co, and Mn (Vidas and Castro 2021; Emam et al., 2024).

The main components of an alkaline electrolyzer cell are illustrated in Figure 3.

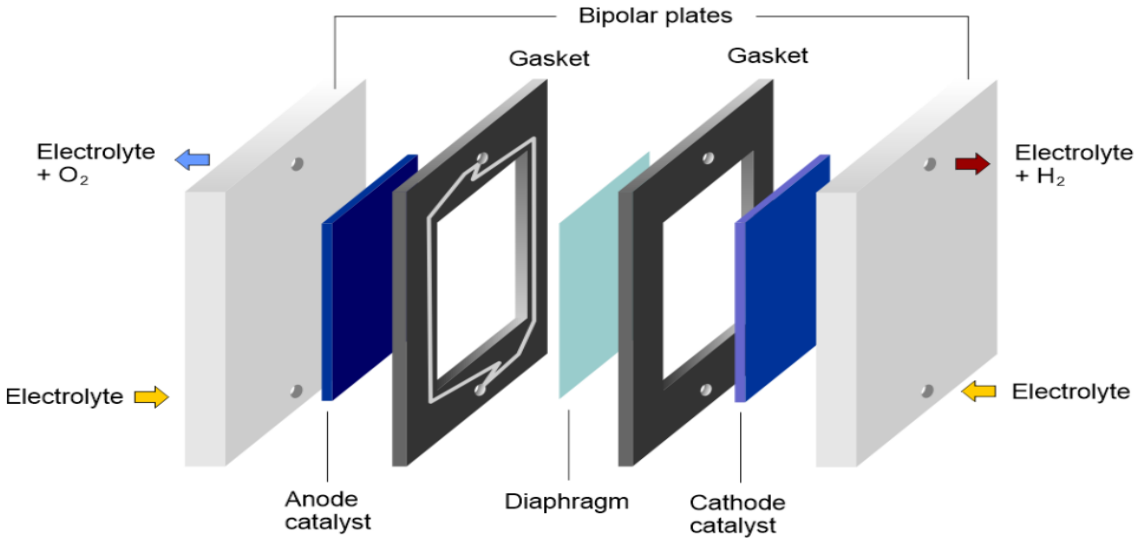

Figure 3: A A-WE electrolyser components

In A-WE, water in a cathodic chamber undergoes an electrochemical reduction reaction on the electrode surface to form hydrogen and hydroxide (OH^-) ions:

$$2H_2O + 2e^- \rightarrow H_2 + 2OH^- \qquad (1.\ 1)$$

(OH^-) ions pass through a diaphragm to the anodic compartment and undergo an oxidation reaction at the electrode surface generating oxygen and water:

$$4OH^- \rightarrow O_2 + H_2O + 4e^- \qquad (1.\ 2)$$

1.2.1. Diaphragm

The diaphragm's function is to separate formed gasses (hydrogen and oxygen) within each cell side to avoid contamination and recombination. It must be impermeable for gases but permeable for water and hydroxide ions. It is important that it has good mechanical and chemical resistance to the highly concentrated potassium-hydroxide solution. A low ohmic resistance is required to avoid increasing the overpotential due to ohmic losses, for this reason, they are made as thin as possible. As explained asbestos have been remplace by composite materials based on microporous polymers or ceramic compounds which are nowadays mainly used. The most widely diaphragm is a polysulfone-based membrane with embedded ZrO_2 particles, commercially known as Zirfon from Agfa. Zirfon is known for its stability in highly concentrated KOH (aq) at temperatures up to 110◦C.

The evolution of A-WE membrane is depicted in Figure 4. The evolution of AWE membranes began in the 1940s with pressurized electrolyzers and asbestos membranes but with their limitations, particularly their swelling properties hindering production efficiency and the health issues , over time,in the 1990s, non-asbestos membranes like Zirfon® membrane were developed, improving efficiency and product purity but had high costs. Finally, the recent prominent advancement is PPS membranes, with lower costs and better stability. When operating the A-WE electrolyzers equipped with a PPS membrane at low voltage, the purity of the product gas still necessitates further enhancement. Recently, (Hu et al., 2024) prepared KOH-doped porous polybenzimidazole membrane, which improves the product gas purity and electrolysis efficiency.

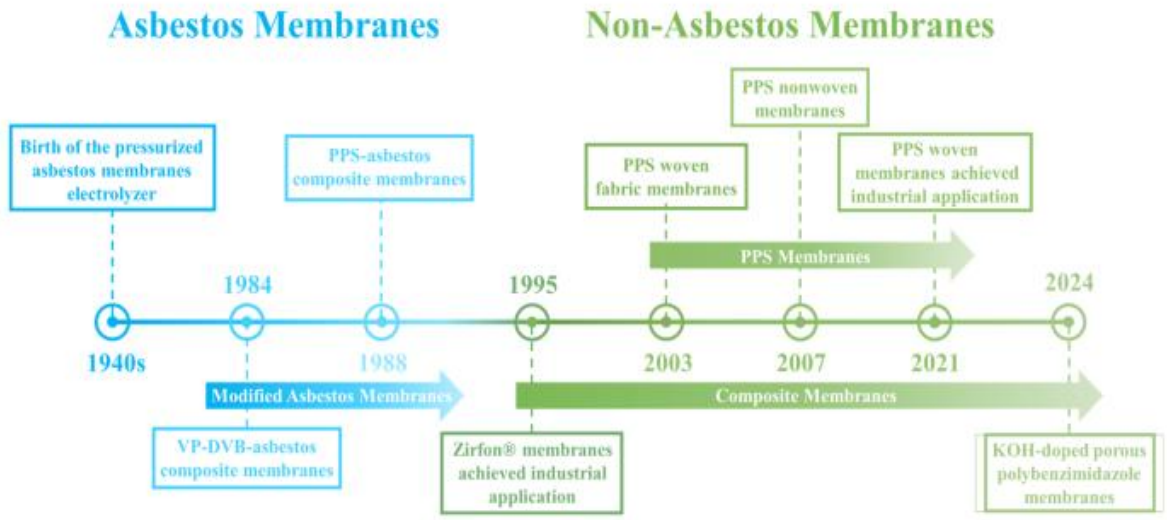

Figure 4: The evolution of A-WE membrane:VP-DVB-asbestos(1984); PPS into asbestos(1988); Zirfon®proposed by AGFA (1995); PPS woven fabric membrane(2003); PPS nonwoven membrane(2007); PPS woven membrane(2021); polybenzimidazole (PBI)-based membrane(2024)

1.2.1. Electrodes

The two electrodes in an electrochemical cell, the anode and the cathode, must be stable, meaning they should not corrode, while allowing electrochemical reactions on their surfaces. These electrodes are typically made of porous materials with complex microstructures, as shown in Figure 5.

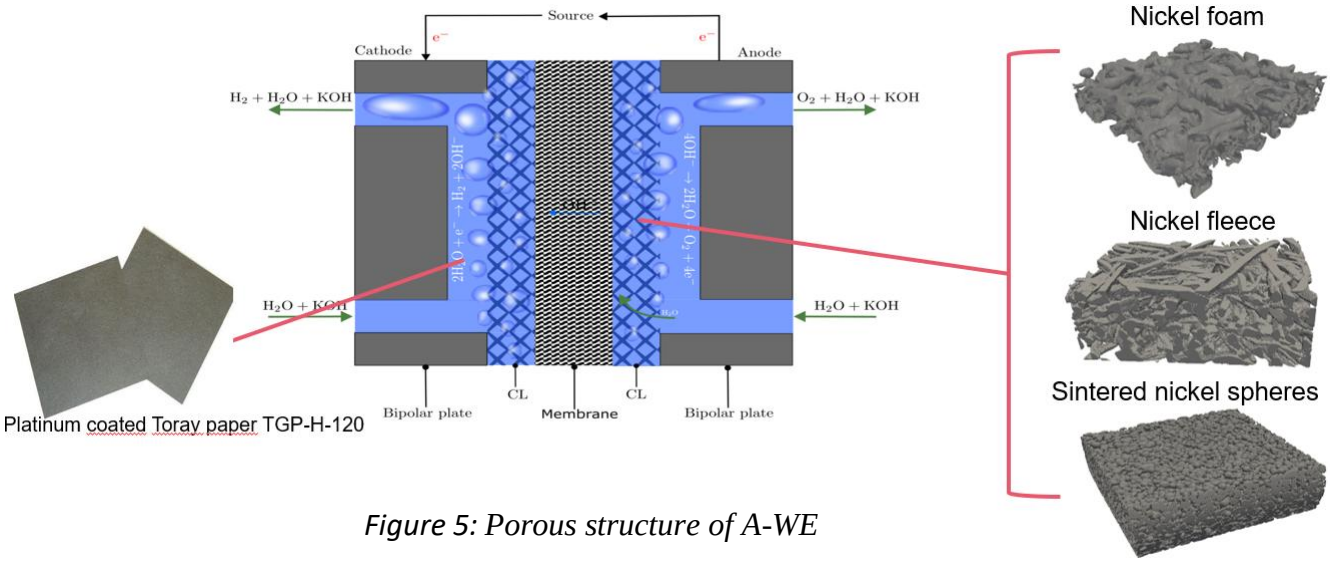

Figure 5: Porous structure of A-WE

The most commonly used substrates in these systems include:

1. Nickel-based substrates

- Sintered Nickel electrode
- Nickel perforated plate
- Nickel foam
- Nickel felt

2. Steel-based substrates

- Stainless steel: types like 316L stainless steel are mostly used for their corrosion resistance and relatively low cost (Russo 2024).

3. Iron-based substrates

- Iron foam or iron plate: iron-based substrates can also be used; however, these require protective layers due to their tendency to corrode in alkaline solutions.

1.3. Progress in A-WE technology

Recent advances in alkaline water electrolyzer cell and stack design have focused on improving materials and architectures to enhance device durability and efficiency. The typical stack configuration consists of series-connected cells separated by bipolar plates, where each cell comprises two half-cells with electrodes and a diaphragm or membrane to minimize gas crossover. At the cell level, several structural modifications have shown significant positive effects in the durability and the efficiency of the cell. These include reducing the gap between electrodes, optimizing electrolyte, improving the microstructure of porous electrodes, and selecting high-conductivity separators. Collectively, these improvements reduce the overall cell resistance, covering both ohmic and activation losses (Campo Schneider *et al.*, 2024).

Performance analyses show that at low current densities, catalytic activity dominates cell performance, whereas at higher current densities, ohmic losses associated with the porous electrode microstructure and separator conductivity become the dominant factors (Campo Schneider *et al.*, 2024). In particular, (Yang et al., 2020) demonstrates that the microstructure of electrodes plays a crucial role in the performance of alkaline electrolyzers operating at high current densities. The porous structure of electrodes directly influences the balance between the active surface area available for electrochemical reactions and the effective removal of hydrogen gas bubbles produced during operation, which are responsible for significant increases in ohmic losses and overpotentials.

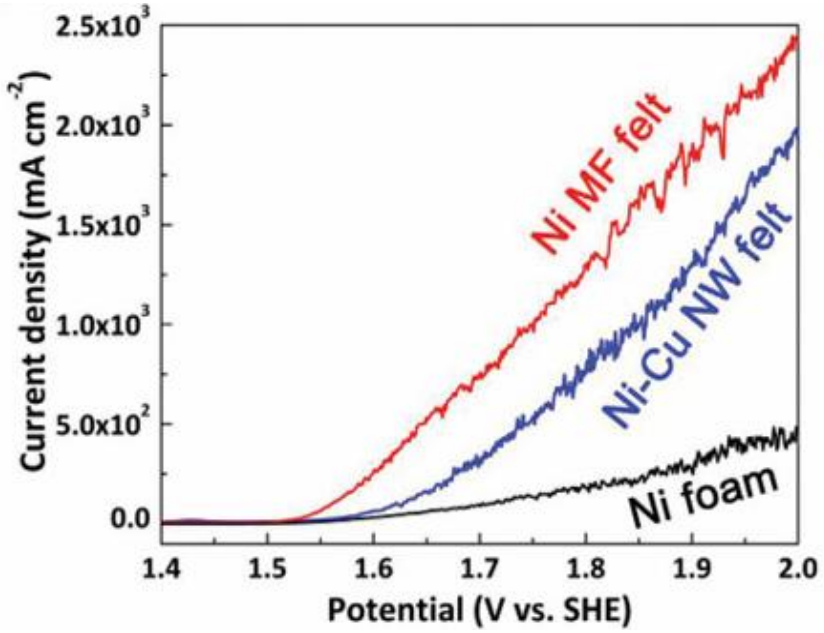

Figure 6: Effects of electrode microstructure on cell performance

The study has compared different types of nickel-based porous structures to evaluate their impact on overpotential and bubble dynamics during water electrolysis, as shown in Figure 6. Linear sweep voltammetry experiments demonstrated that nickel microfiber felts(Ni MF felt) exhibited lower overpotentials (330 mV at 100 mA·cm⁻²) compared to Ni–Cu nanowire felts (Ni-Cu NM felt) (390 mV), despite having ~25% lower specific surface area. This highlights that pore morphology and bubble management are as important as the active surface area in determining electrochemical behavior.

Pulsed electrolysis experiments confirmed this trend: although Ni–Cu NW felt initially showed lower overpotentials, they rapidly increased (within one minute) due to enhanced bubble trapping within the porous media. This phenomenon was attributed to the high ratio between bubble diameter and pore-throat diameter, which favors bubble retention. In contrast, nickel foams, with their large pores and throats, showed almost no bubble trapping, but displayed higher overpotentials (470 mV at 100 $mA \cdot cm^{-2}$) due to their relatively low surface area.

These findings suggest that Ni microfiber felts represent an optimal compromise between surface area and bubble removal. An alkaline flow electrolyzer using such electrodes sustained an impressive current density of 25 $A \cdot cm^{-2}$ for 100 hours, which is approximately 12.5 and 50 times higher than conventional alkaline and PEM electrolyzers, respectively. Moreover, this value is 6.4 times greater than the best performance previously reported in the literature (Yang et al., 2020). Such productivity gains are particularly advantageous for reducing the cost of green hydrogen.

This strong relationship between microstructure and performance underscores the need for a precise understanding of the transport mechanisms within the porous microstructure. Deep understanding of these phenomena is essential to guide the design and optimization of electrodes to maximize energy efficiency, limit losses, and enhance system durability and performance.

Conclusion

This literature review has highlighted significant advancements in the field of alkaline water electrolysis. The development of materials, particularly separator membranes and electrodes, has been identified as a key driver for improving performance, and the purity of the produced gases. A good understanding of the interactions between electrode microstructure and transport phenomena has been shown to be essential for system optimization. These technological improvements appear promising for addressing current energy challenges, especially in the context of large-scale green hydrogen production.

Chapter 2

Material and methods

Introduction

As discussed in the introduction, the goal of this thesis is to use PNM approch to estimate transport properties of A-WE porous electrode from X-ray macrotomography images and compare with CFD simulation. This chapter describes the materials and methodologies used for image acquisition, processing, network reconstruction and transport simulation (CFD and PNM).

2.1. Materials

The sintered Nickel sphere used as an electrode in an alkaline electrolysis cell have been studied. To understand the internal structure of this material, an advanced imaging technique called X-ray microtomography is employed, which provides high-resolution images enabling solid and porous phases to be distinguished. As we can see in Figure 7, an X-ray microtomography scanner was used to obtain a detailed three-dimensional representation of the porous morphology of the sintered Nickel spheres. The sample is placed in the scanner, then the device acquires many 2D X-ray radiographs from different angles, and a computer reconstructs these projections into a precise virtual 3D image of the interior of the sample(Jung, 2020).

The µCT image reconstruction is then used to extract the pore network using porespy, an open-source Python designed for pore network extraction from 3D images of porous media before performing the transport simulation with PNM after image processing.

2.2.

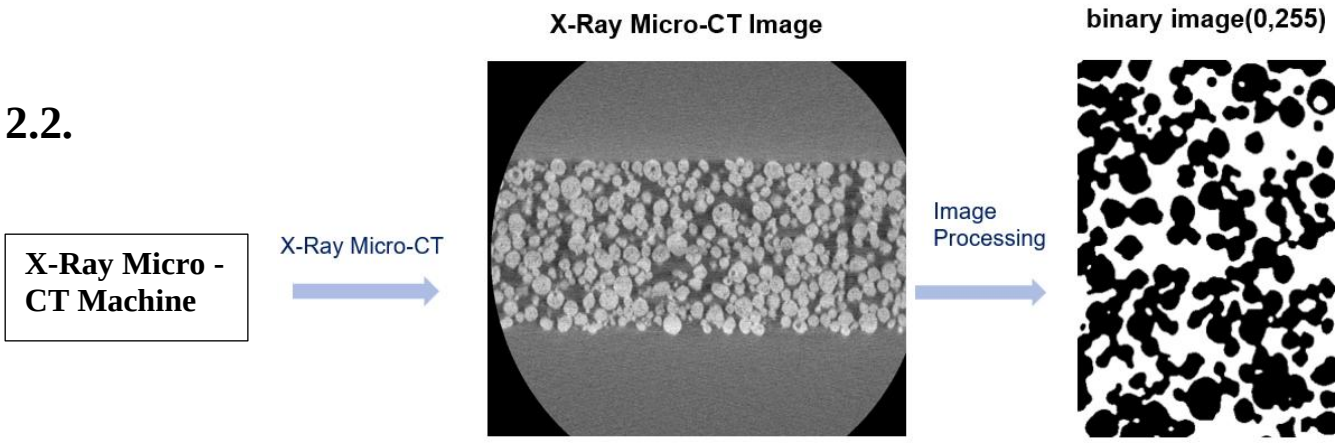

Figure 7: Step for obtaning binary microstructure ready for simulation

Methodology

After obtaining the μCT image reconstruction, image processing is performed to convert it into a binary format, where solid regions are represented by black pixels with a value of 0 and pore regions by white pixels with a value of 255. Since PoreSpy requires a normalized binary image with values 0 and 1 for solid and pore regions, the binary image with pixel values 0 and 255 is normalized to 0 and 1 before extracting the network and performing the transport simulation. In the following subsection, the pore network extraction and transport simulation are described.

The diagram in Figure 8 illustrates the workflow starting from micro-CT imaging of the porous media, followed by image processing to obtain a binary image and the transport simulation. This workflow highlights steps for simulating transport phenomena in porous media using both CFD and PNM approaches.

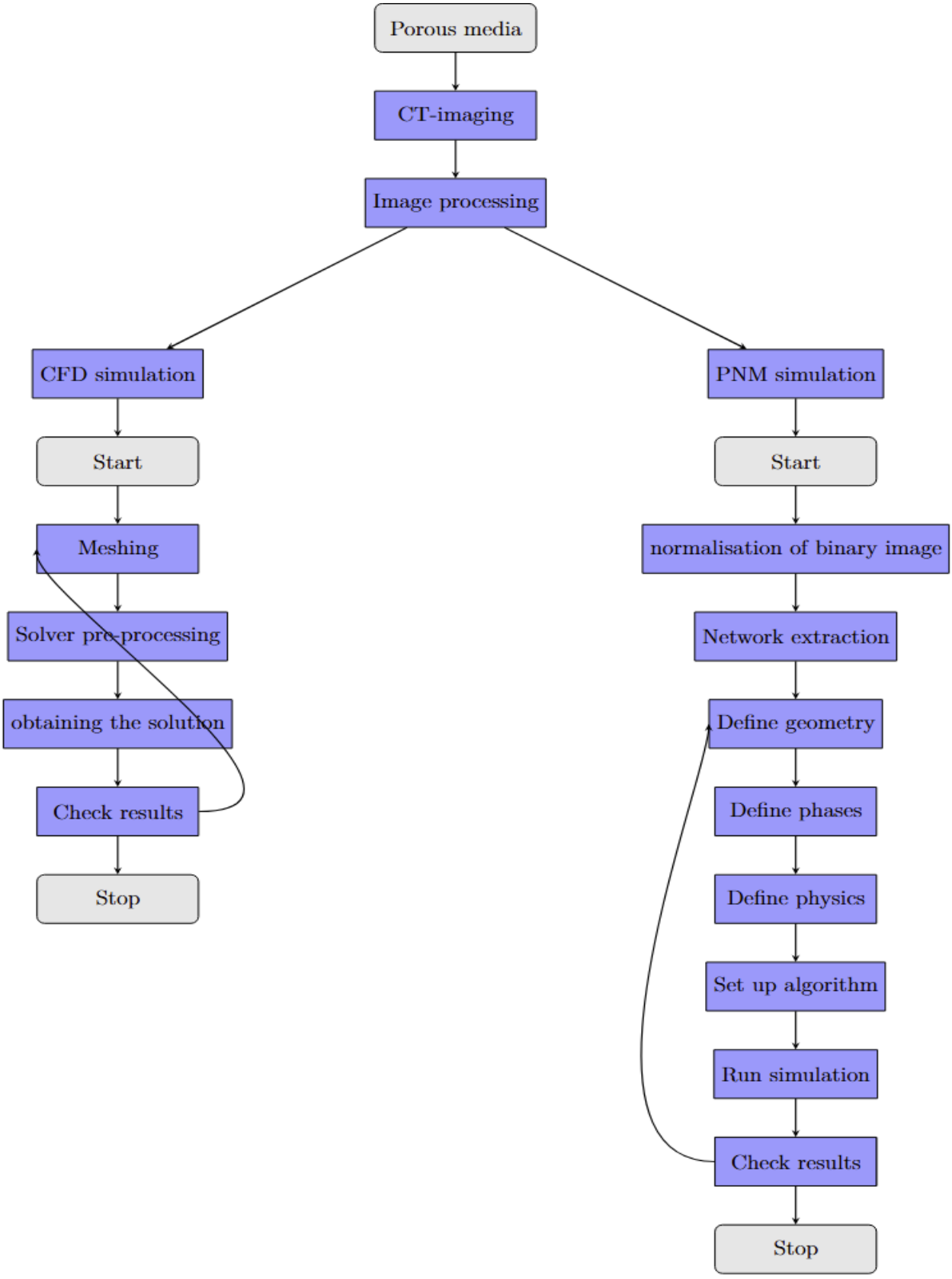

Figure 8: Process outline from binariry image to CFD and PNM simulation

2.2.1. Computational fluid dynamics (CFD)

The fundamental objective of Computational Fluid Dynamics (CFD) is to obtain numerical solutions to the governing partial differential equations (PDEs) that describe fluid flow and related transport phenomena. A widely adopted discretization technique in CFD is the Finite Volume Method (FVM), which transforms the continuous PDEs into a system of algebraic equations. These equations are typically solved iteratively to approximate the flow field and other dependent variables. The mathematical formulation of the FVM, particularly prevalent in fluid mechanics, is based on the solution of the fundamental conservation laws for mass, momentum, and energy. Unlike in solid mechanics, where balance equations are typically expressed for material points (Lagrangian framework), in fluid mechanics they are formulated for spatially fixed, open control volumes (Eulerian framework), through which fluid continuously flows. This approach is necessitated by the inherent difficulty of tracking individual fluid particles in a flow domain (Ferziger et al.,2002). The connection between these formulations is established via the Reynolds Transport Theorem, which defines the link between the Lagrangian and Eulerian descriptions of continuum mechanics. Within the FVM framework, the temporal rate of change of a conserved quantity within a control (CV) volume is determined by the net sum of convective and diffusive fluxes across its boundary surfaces, as well as by any volumetric sources or sinks within the domain. In the following, this principle is examined in greater detail using the integral form of the governing equations. All relevant conservation laws can be expressed in the following general integral formulation (Böhme, 2000; Moukalled et al., 2016):

$$\iiint_V \frac{\partial(k\rho)}{\partial t} dV + \underbrace{\iint_S \rho\, ku \cdot n dS}_{convective\ flux\ term} = \underbrace{-\iint_S j \cdot n dS}_{diffusive\ flow\ term} + \iiint_V \sigma\, dV \qquad (2.\ 1)$$

Here k represents the specific quantity transported with the mass, j the specific diffusive flux density, σ the volume-specific production rate and ρku the convective flux density. Furthermore, ρ is the density of the fluid, t the time, V the volume resp, S the surface of the CV and n the unit vector perpendicular to the surfaces. The balance quantity transported with the mass in the mass balance is the mass itself, so that $k = 1$ applies and the mass balance is calculated as:

$$\iiint_V \frac{\partial \rho}{\partial t} dV = -\iint_S \rho\, u \cdot n dS \qquad (2.\ 2)$$

According to this, the change of mass inside the CV corresponds to the change of density over time and the mass flow through the surface. The momentum balance results from the substitution of the velocity as a specific balance quantity $k = \mathrm{u}$, by $\mathrm{j} = \mathrm{S}$ and $\sigma = \mathrm{f}$:

$$\iiint_V \frac{\partial(\rho \mathbf{u})}{\partial t} dV = -\iint_S u\,\rho(u \cdot n) dS + \iint_S S \cdot n dS + \iiint_V f\, dV \qquad (2.3)$$

According to this, the change in momentum within the CV results from the sum of the convective momentum flux over the surfaces, the surface forces due to diffusive influencing quantities and the volume forces. f represents the mass density and S is the Cauchy stress tensor which, assuming a Newtonian fluid, can be divided into an isotropic normal stress fraction represented by the static pressure p and a fraction consisting of the shear stresses according to

$$S = -pI + T. \qquad (2.4)$$

The shear stress tensor T for Newtonian fluids is determined by the following rheologically linear approach

$$T = 2\eta D + \eta_v (tr(D))I \qquad (2.5)$$

consisting of the strain velocity tensor D, the dynamic viscosity η and the volumetric viscosity η_v. These equations are known as the Navier-Stokes equations.

2.2.2. Pore network modeling approach

Pore network modeling is an efficient approach to simplify the computational procedure to simulate multiphase transport. The fundamental idea behind pore network modelling is to map the phase of interest into a connected network of nodes and edges. In porous electrodes, the void space is mapped to a connected network of pores and throats corresponding to wide voids and narrow constrictions, respectively. Therefore, PNM simplifies the void space with smaller amount of information about pore geometry (e.g. radius, volume) and topology (e.g. coordinates, connections) (Sheng, 2013). Such simplification is the main reason for lower computational cost of PNM. Therefore, PNM is advantageous in contrast to CFD in terms of computational cost, especially in larger samples and where multiphase and more complex physics are involved. Electrochemical modeling of porous electrodes using PNM includes modeling fluid flow to find the distribution of velocity and pressure throughout the network,

followed by solving the systems of mass and charge transport to find the species concentration and electrical potential within the network. In this section, more details on PNM approach are provided.

2.2.3.1. Pore Network Extraction

The first step of the PNM simulation is defining a network that can represent the material of interest. Obtaining a network can be done either generating an artificial network or extracting one from a binary image stack (Misaghian, 2022; Jung, 2020). Examples of a generated cubic network and an extracted network are shown in **Error! Reference source not found.** In generated networks, the network connections and geometry are generated using standard networks such as Cubic lattice, Delaunay, and Voronoi. Geometrical data, such as pores and throat sizes, are assigned to the network elements to represent an arbitrary or real material's pore size distribution. Although generated networks do not capture the real connectivity of the void space, they can be used as a good approximation of the porous medium when the porous sample's image is not available. However, extracted networks from real image data are advantageous for capturing void space connectivity, topology, and geometry, enabling better structural-performance analysis (Gostick, 2017).

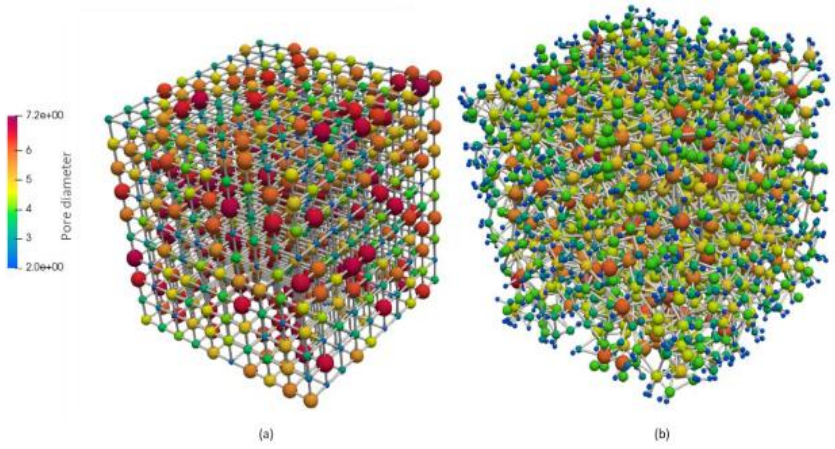

Figure 9: a) A generated cubic network b) An extracted network

Pore network (PN) extraction from X-ray tomographic (CT) images is carried out using three main methods: the medial axis, the maximal ball and the watershed segmentation. Alongside these direct

methods, alternative optimisation and hybrid approaches like SNOW2 algorithm have emerged. These approaches aim to combine the strengths of the three main methods while overcoming their respective limitations.

2.2.3.2. Medial axis method

The medial axis method aims to extract the "skeleton" of the pore space from 3D image. This skeleton, or medial axis, represents the central paths of the void, which allows the topology and connectivity of the pore network to be captured.

The process start with calculating the Euclidean Distance Transform (EDT) on volumetric data. For each point in the pore, we measure the distance to the nearest solid surface. The points where this distance is maximum and where there are at least two points on the boundary at the same distance are selected; these are the centers of the maximum spheres. Followed by a thinning algorithm that scans foreground voxels in ascending order of distance from the solid boundary and deletes as many non-essential voxels as possible without altering the network's connectivity. This approach accelerates the thinning process and ensures that the resulting medial axis strictly preserves the topological features of the pore structure(Wang et al., 2019).

In the resulting skeleton, junctions are the centers of the maximum spheres, and the radius of each pore is defined as the local distance from the junction to the nearest solid boundary. The segments connecting these junctions are considered as throats (Wang et al., 2019).

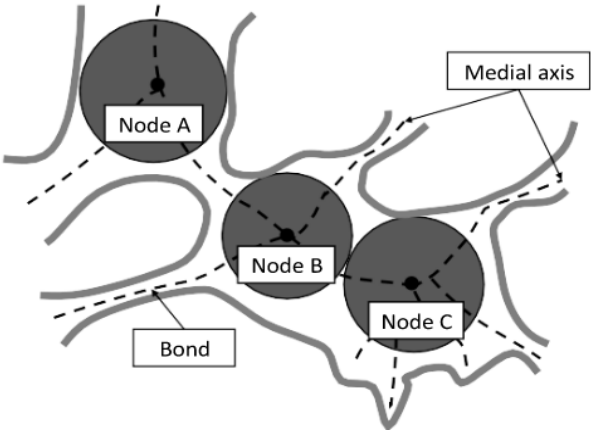

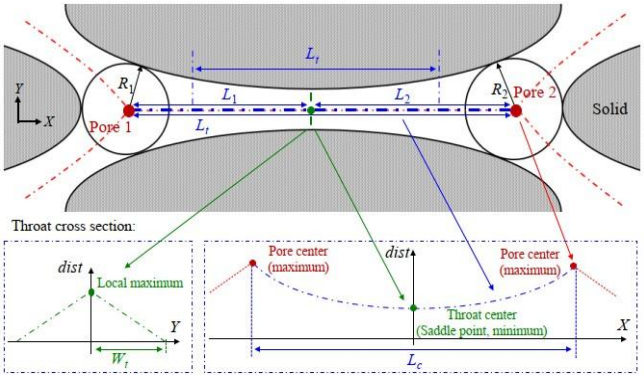

Figure 10: Illustration of the medial axis method

However, the medial axis is sensitive to surface irregularities, which can generate redundant connections. Therefore, further elimination processes are necessary to remove these inessential connections, though eliminating redundancy remains challenging. As a result, while the medial axis method is attractive for preserving the basic topological and morphological properties of the pore space, it can sometimes lead to ambiguous pore identification due to the persistence of redundant links and overlapping nodes (Yi et al. 2017). Figure 10 and 11 illustrate the medial axis method and its sensitivity to surface irregularities.

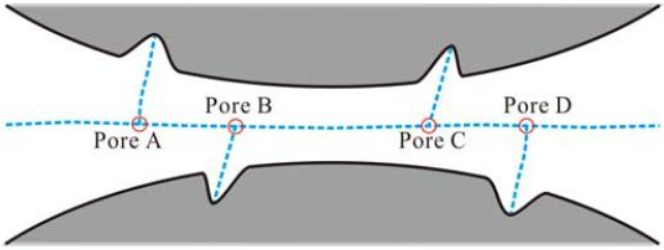

Figure 11: Illustration of the sensitivity of medial axis to irregularities on the grain surface

2.2.3.3. Maximal ball method

In the maximal ball method, each void voxel is first set with the largest inscribed sphere. Eliminating processes are then performed to remove those spheres that are subsets of others. The remaining spheres are called maximal balls. Thereafter, clustering processes are applied to organise the maximal balls into pore–throat chains according to their sizes and ranks. In general, pores are the largest spheres centered in the pore spaces of porous media, and their diameters are defined as pore diameters. Throats are composed of a series of small spheres connecting two pores, and the maximum diameters of the connecting spheres are defined as throat diameters. The irregularity in the geometries of real pores and throats is considered by introducing the dimensionless shape factor G, which is defined as the ratio between the cross-sectional area A and the square of perimeter P, i.e., G = A/P2.

The main advantage of the maximal ball method is that it can capture the wider pore space region corresponding to the geometrical pores, and the concept is easy to understand.

However, there are still some minor problems related to the maximal ball method. This method tends to find too many small pores and throats, which are nderestimate the pore size. In addition, this method is likely to underestimate the length of throats when the pore throat chain is tortuous, see Figure 12. The reason is that the maximal ball method uses Euclidean distance between the centre of pores and the throat to define the lengths. Again, the other problem is the distinction between pores and throats, where some arbitrary criteria are used to partition the pore space (Li et al. 2021).

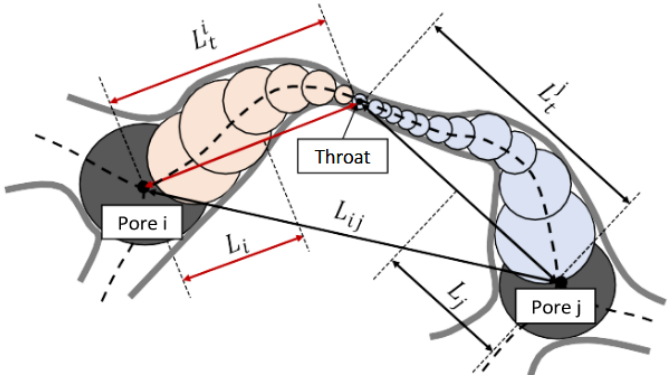

Figure 12: Schematic of the lengths of pores defined by the maximal ball method

2.2.3.3. Watershed segmentation method

Watershed segmentation of void space was firstly studied by Thompson et al. and Sheppard et al. over ten years ago (Wang et al., 2019). Recently, this method has received more attention. Watershed segmentation utilizes the distance map of the void space, which is defined as the distance from the center of each pixel in void space to the nearest pixel on solid space. Watershed segmentation transforms the void space based on the distance map into catchment basins, which comprise all points whose path of steepest descent terminates at the local minimum. The identified watersheds or surfaces of minimum distance represent the throats, and the catchment basins are the pores. All the pore volume is assigned to pore and throats are surfaces that define the boundary between two pores.

The main advantage of the watershed segmentation method is its efficiency in constructing pore networks. However, it is less reliable when dealing with sheet-like pores where the distance map is not a good representation of the void space. In addition, watershed segmentation is sensitive to surface roughness, which creates spurious local maxima and leads to the over-segmentation problem, particularly

in high-porosity materials and overestimates pore density. The method also needs user supervision and is hard to apply in automatic pore space segmentation.

2.2.3.5. SNOW network extraction (Sub-Network of Over-segmented Watershed)

Recently, Gostick employed the marker-based watershed segmentation (SNOW) to extract pore networks (Gostick et al., 2016). SNOW algorithm applies several improvements to eliminate the spurious or erroneous peaks (local maxima in the distance map), which cause the over-segmentation problem in the simple Watershed segmentation method.

The main idea of the SNOW algorithm is to find a suitable set of initial markers in the image so that the watershed is not over-segmented.

2.2.3.6. SNOW2 algorithm

The SNOW algorithm uses a standard marker-based watershed segmentation function to identify pores. Finding peaks in the distance transform which truly correspond to pore centers requires several careful steps. Each of these steps can be done manually, but the SNOW2 function was created to combine them all in a single function for ease of use.

In addition to the original SNOW algorithm, SNOW2 also incorporates a few new developments such as multiphase extractions and parallelized processing. The new snow2 function also handles boundaries better and returns a different set of geometrical properties. For instance, it no longer returns the attribute ‘pore.diameter’, which was an opinionated choice that was not appropriate for every case. Instead it returns several different diameters, like ‘pore.equivalent-diameter’ and ‘pore.inscribed-diameter’, and the user must decide which of these they wish to declare as the real ‘pore.diameter’.

In this work, the SNOW2 algorithm is used to extract the PN. On the binary image, a distance transform map is created by replacing each void pixel with their distance value from nearby solid. Distance maps create cloud-like shapes that are denser in the centers shown as peaks of the distance

transform. Applying a maximum filter on distance map locates the distance peaks as centers of pore regions. An algorithm to find and remove spurious peaks is then applied to prevent over-segmentation. The resulting peaks are then used as markers for finding the basins of the distance map and segmenting the pore regions in a marker-based watershed segmentation algorithm.

The network model is then extracted from the segmented image, in which each region corresponds to a pore and their connecting channels are considered as throats. This is the description of the different step in SNOW2 algorithm but PoreSpy includes a predefined function called SNOW2 that applies all the steps automatically and we apply that function on our binary image to extract the Pore Network.

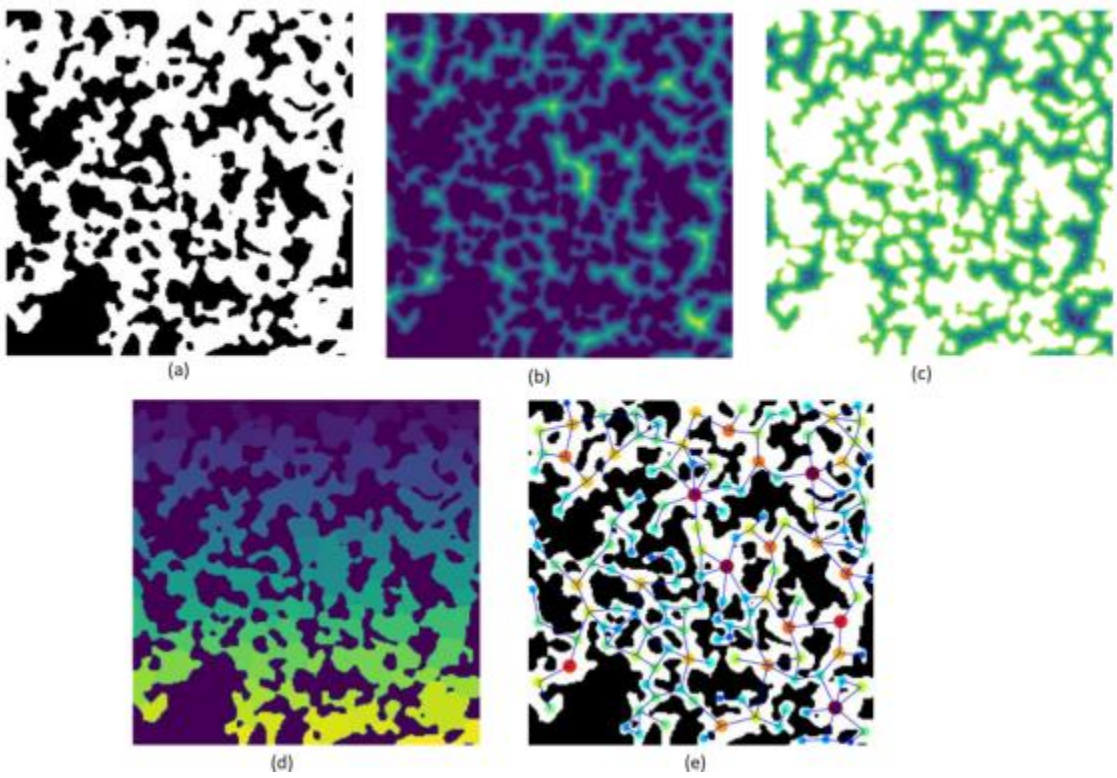

Figure 13: Illustration of the main steps in SNOW algorithm for a 2D randomly generated porous medium. a) The binary image of a randomly generated porous medium b) Distance map of the void space c) Peak points for watershed basins are shown as white dots within the distance map d) Segmented regions based on the watershed method e) The extracted network mapped on the binary image.

2.3. Transport equations used in PNM

The transport processes in pore network models are modeled by applying the governing equations in a network of connected pores and throats. The region extending from the center of one pore to the center of its neighboring pore is referred to as a *conduit element*, and its conductance for transport phenomena is incorporated into the system of equations in PNM Since this thesis focuses on modeling transport phenomena under steady-state conditions, the PNM formulations presented in this section are developed accordingly. For steady-state Stokes flow, assuming a Newtonian and incompressible fluid, the mass conservation around pore *i* can be expressed as follows:

$$\sum_{j=1}^{N_i} q_{ij} = \sum_{j=1}^{N_i} G_{ij}^{h} (P_i - P_j) = 0, \quad i = 1,2, \dots, N_p \tag{2.6}$$

where j is the number of neighbors of pore i and q_{ij} is the flow rate between pore i and pore j. G_{ij}^{h} is the hydraulic conductance of the conduit element ij and N_p is the total number of pores in the network. G_{ij}^{h} can be estimated using the resistors-in-series method from the conductance of each conduit's element. For transport "tr", the conduit conductance is calculated as follows:

$$\frac{1}{G_{tr,ik}} = \frac{1}{g_{tr,i}^{p}} + \frac{1}{g_{tr,ik}^{t}} + \frac{1}{g_{tr,k}^{p}} \tag{2.7}$$

The conductance of each element depends on the transport properties (e.g. fluid viscosity in hydraulic transport) and geometrical properties of the element (e.g. diameter, length). For fluid flow transport assuming a cylindrical throat, the throat conductance can be defined from the analytical solution of steady-state Navier-Stokes equations for flow in a cylindrical pipe, resulting in the Hagen-Poiseuille equation as follows(Misaghian, 2022):

$$g_{h,ij} = \frac{\pi d_{ij}^{4}}{128\, \mu\, l_{ij}} \tag{2.8}$$

where d_{ij} and l_{ij} are the diameter and length of throat ij, and μ is the dynamic viscosity of the fluid.

Modeling a Stokes flow problem in a pore network involves solving a system of linear equations, resulting from applying equation

$$\sum_{j=1}^{N_i} q_{ij} = \sum_{j=1}^{N_i} G_{ij}^{h} (P_i - P_j) = 0, \quad i = 1,2, \dots, N_p$$

(2.9)

to find the unknown pressure values in each pore. It can now be clearly seen that the accuracy of defining G_{ij}^{h} highly affects the accuracy of the simulation.

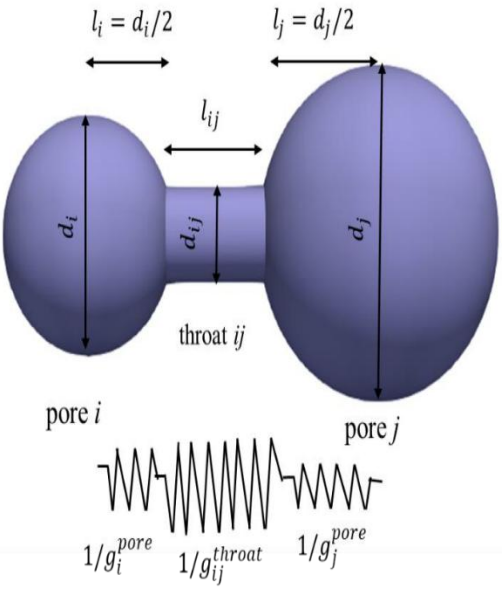

Figure 14: A schematic of a pore-throat-pore element in PNM

2.4. Calculation of the geometric properties of the extracted network

In this study, the porosity and the specific surface area were determined from the extracted pore network.

The porosity p is calculated as the ratio between the total pore volume and the total domain volume:

$$p = \frac{V_{pore}}{V_{total}} \qquad (2.10)$$

where the total pore volume is given by:

$$V_{pore} = \sum_{i=1}^{N_p} V_{pore,i} \qquad (2.11)$$

with $V_{\text{pore},i}$ being the volume of pore i, available in the dictionary and the total pore volume is obtained by using:

$$V_{pore} = np.sum(net['pore.volume']) \quad (2.\ 12)$$

The specific area per volume is obtained by using the pore.surface-area also available in the network.

$$SSA = \frac{S_{total,pore}}{V_{total}} \quad (2.\ 13)$$

where the total pore surface area is given by:

$$S_{total,pore} = \sum_{i=1}^{Np} s_{pore,i} \quad (2.\ 14)$$

with $S_{\text{pore},i}$, the surface area of pore i

$$S_{total,pore} = np.sum(net['pore.surface\text{-}area']) \quad (2.\ 15)$$

Conclusion

In this section, the material used in the research, a sintered nickel electrode was described. The SNOW2 algorithm was explained as the method employed for extracting the pore network from the µCT image. Additionally, the extracted network geometric properties calculations and the two numerical approaches: Pore Network Modeling (PNM) and Computational Fluid Dynamics (CFD), for transport simulation were presented.

Chapter 3

Results and discussion

Introduction

This section presents and analyzes the results obtained from the extraction of pore networks and transport simulations. The pore network extraction was performed from binary µCT images of sintered Nickel using the SNOW2 algorithm. The objective is to assess the fidelity of the extraction by comparing geometric properties such as porosity and interfacial area per volume with real image analysis data. This step is crucial to ensure the accuracy of the simulation models. Subsequently, single-phase flow simulation were conducted using both pore network modeling and computational fluid dynamics. The comparison between these two simulation approaches provides a critical evaluation of PNM's capability to faithfully represent the complex physical phenomena within porous electrodes, while considering computational performance.

3.1. Reconstruction of pore networks

3.1.1. Extracted network

The pore network extraction from the µCT binary images was performed using the SNOW2 algorithm implemented in OpenPNM The resulting network dictionary, shown in Table 1 contains comprehensive geometrical and topological properties.

Table 1: Results of snow2 generated

Network	Dictionary with 30 items
Regions	Array of size (976, 882, 348)
Phases	Array of size (976, 882, 348)

The network was opened with OpenPNM and inspected to identify the extracted properties.

The 30 items of our dictionary in Table 1 include properties like pore coordinates, inscribed diameters, throat lengths, and connectivity information and the labels which enable easy retrieval of a list of important pores (or throats), such as pore.boundary. This dictionary is the core of the mathematical and computational representation of the network. The extracted properties will serve to calculate any other geometrical properties of the porous medium. The regions and phases size (976, 882, 348) imply a high resolution of segmentation and phase distribution of the porous material because the size is close to the real size of our binary image (971, 876, 343), which limits the risk of information loss due to under-segmentation. The small difference can be due to the automatic addition of boundary pore during the network extraction to facilitate border management during network segmentation and extraction. This helps avoid edge effects and better define regions close to the image contour.

Table 2 and Table 3 highlight the set of properties and labels extracted from the reconstructed network, covering both pore and throat. The extracted network consists of 29175 pores and 75553 connections(throats), representing the complex porous microstructure of the sintered nickel electrode. Each pores and throat has its own different properties in the dictionary and is described by a collection of geometric, topological, and physical parameters. The boundary pores are 4511, divided into pores. xmin and pore. xmax in each direction.

Table 2: Network properties

#	Properties	Valid Values
1	throat. conns	75553 / 75553
2	pore. coords	29175 / 29175
3	pore. region_label	29175 / 29175
4	pore. phase	29175 / 2175
5	throat. phases	75553 / 75553
6	Pore.region_volume	29175 / 29175
7	pore. equivalent_diameter	29175 / 29175

8	pore. local_peak	29175 / 29175
9	pore. global_peak	29175 / 29175
10	pore. geometric_centroid	29175 / 29175
11	throat. global_peak	75553 / 75553
12	pore. inscribed_diameter	29175 / 29175
13	pore. extended diameter	29175 / 29175
14	throat. inscribed_diameter	75553 / 75553
15	throat. total _ length	75553 / 75553
16	throat. direct _ length	75553 / 75553
17	throat. perimeter	75553 / 75553
18	pore. volume	29175 / 29175
19	pore. surface_area	29175 / 29175
20	throat. cross sectional area	75553 / 75553
21	throat. Equivalent_diameter	75553 / 75553

Table 3: Network labels

#	Labels	Assigned Locations
1	pore. all	29175
1	Throat.all	75553
2	pore. boundary	4511
3	pore. xmin	495
4	pore. xmax	491
5	pore. ymin	495
6	pore. ymax	498
7	pore. zmin	1476
8	pore. zmax	1056

Connectivity and Spatial Structure: throat.conns identifies connections between pores, ensuring the network's topological completeness with no missing links. pore. coords and pore. geometric-centroid denotes the spatial positioning and the geometric centre of each pore, allowing for visualisation and quantitative analysis of the pore space.

Size and Shape Descriptors: properties such as pore.equivalent-diameter, pore.inscribed-diameter, pore. extended-diameter provides measures of the pore size using various shape-based definitions. Similarly, throat. inscribed-diameter and throat. equivalent diameter describes the size characteristics of the throats, important for transport modeling. The diversity in sizes and shapes of pores and throats reflects the heterogeneous nature of the medium, a key factor influencing absolute permeability and tortuosity

Volume and Surface: pore.volume and pore.surface-area gives insight into the storage and interface capacity of each pore, which are fundamental parameters affecting porosity, fluid flow and reactive processes.

Throat Geometry: Metrics throat. total-length and throat.direct-length, throat.perimeter, and throat.cross-sectional-area to ensure that the network faithfully represents the connections between pores, capturing the main channels for transport phenomena.

The assignment of specific labels to boundary pores according to different spatial directions facilitates the definition of boundary conditions in the transport simulations. This information is crucial for accurately reproducing real flows. Having access to multiple geometric properties enables us to calculate the porosity and the specific area per volume for comparison with the experimental data for the evaluation of the reconstructed network, and to plot the pore size distribution.

We then calculate the porosity and the surface area per volume of the network by using the formula in the methodology section. dividing the total pore volume to the volume of the image.

After computing the porosity and the specific area per volume, we visualize the network, in Figure 15 and the pore size distribution, in Figure 16. For the visualisation, we assume the pores to be spherical and the throats cylindrical.

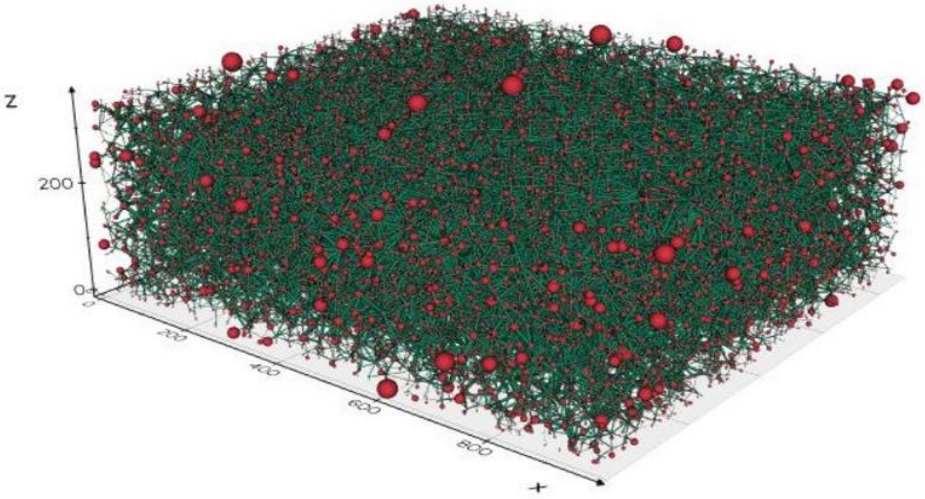

Figure 15: Reconstructed network of Sintered Nickel electrode

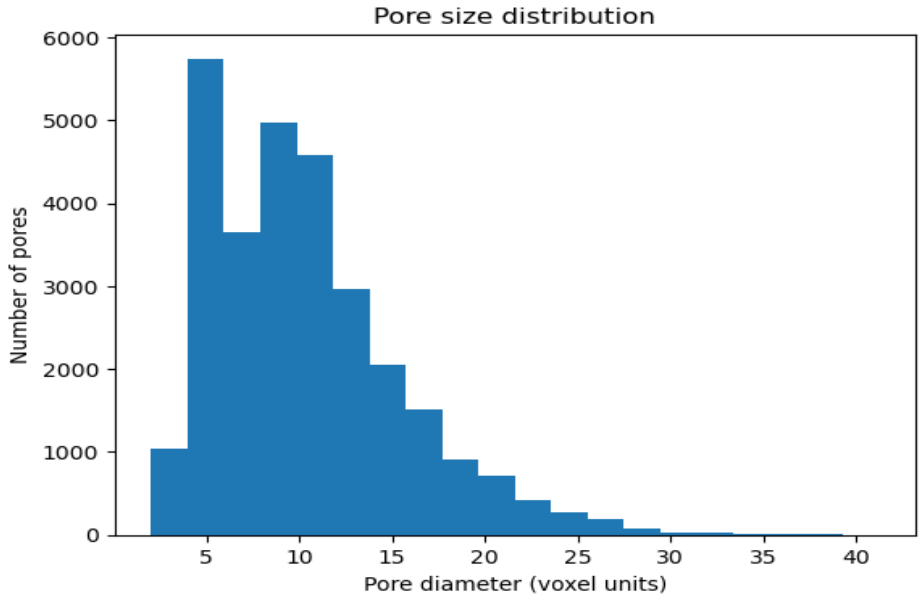

Figure 16: Pore size distribution

3.1.2. Comparison of geometric properties of extracted network with image analysis results

The porosity obtained from the extracted pore network 0.453, is very close to the value obtained from direct image analysis, 0.445, with a minimal error of 1.79% as shown on Table 4. Pore network porosity followed almost a 1:1 relationship with image porosity, indicating that the reconstruction preserves the quantitative pore structure with high fidelity. This precision in porosity prediction is

consistent with findings in the literature, where pore network extraction methods usually reproduce porosity values close to the results of image analysis.

Table 4: Comparison of Porosity

Extracted Pore Network	**Experiment**	**Error (%)**
0.453	0.445	1.79

The difference between the interfacial area per volume from extracted network and image analysis is about 11% as shown on Table 5, demonstrating a correspondence between the reconstructed network and the physical reality of the porous material. Such close agreement highlights the effectiveness of extraction algorithms in accurately preserving the complex structure of pore-solid interfaces, which are crucial for multiphase transport, mass exchange, and surface reactions.

Table 5: Comparison of interfacial area per volume

Extracted Pore Network	**Experiment**	**Error**
$0.098\ m^{-1}$	$0.109\ m^{-1}$	$10.09\ m^{-1}$

The comparison in Tables 4 and Table 5 confirms strong similarity between the extracted network and the actual microstructure, indicating that the SNOW2 algorithm preserves essential geometric features

In conclusion, the close agreement between the pore network reconstruction and image analysis value of both porosity and interfacial area per volume demonstrates that the reconstruction method reliably captures the essential geometric characteristics of the porous material and validates the relevance of the PNM approach for geometric properties analyses. These findings agree with previous studies validating the accuracy of SNOW2 extracted method (Gostick et al., 2016; Huang et al., 2020). This fidelity in representing the microstructure is a critical prerequisite for accurate modelling. The next

logical step is to leverage this detailed pore network model to perform single-phase flow simulations, which will enable further investigation of transport properties and validation of the network's predictive capabilities under realistic flow conditions.

3.2. PNM Simulation

3.2.1. Predicting permeability in PNM

Permeability of a porous medium is an intrinsic parameter that indicates how easily fluid can flow through the medium. Permeability of porous electrodes is a characteristic of the electrodes and can be used as a validation parameter for comparing the accuracy of a PNM with experimental values or CFD methods. To find the permeability of a porous electrode using PNM, a flow algorithm can be applied with a pressure gradient boundary condition. Once the flow rate values are found from the solution of the algorithm, the permeability (K) can be calculated using Darcy's law as follows:

$$K = \frac{Q}{A}\frac{\mu L}{\nabla P} \qquad (3.2)$$

where Q is the volumetric flow rate , A is the cross-sectional area of the porous domain , L is the distance between inlet and outlet, μ is the fluid viscosity, and ∇P is the pressure gradient along the direction of flow.

As explained in the material and methods section, the accuracy of conduit conductance values within the network affects the accuracy of PNM results. Hydraulic conductance estimation using the Hagen-Poiseuille equation 2.8 was developed for fluid flow in cylindrical elements. However, in extracted networks like in this case, original pore regions from the porous medium image have irregular shapes, and cylindrical pore and throat elements may not be the best representative of the real geometry's conductance and the intrinsic geometric complexity of porous materials makes it difficult, if not

impossible, to choose a priori, which geometrical model will best represent the pores and throats in the material.

The conductance of each throat is directly related to its geometry as well as that of the connected pores, which significantly influence the flow rates equation 2.6 and, by extension, the overall permeability of the material equation 3.7. This sensitivity to geometry and the complex intrinsic geometry of the material arises from the use of different geometrique models available in open PNM to estimate the hydraulic conductance and then the permeability as shown in Table 6.

Table 6: permeability with different geometries (pores and throats)

Geometric models	**Permeability (m^2)**
Cones and cylinders	1.671e-12
Cubes and cuboids	7.247e-12
Pyramids and cuboids	2.586e-12
Squares and rectangles	8.823e-13
Trapezoids and rectangles	3.791e-13

A regular pressure gradient is observed in Figure 17, from high pressure at the inlet to low pressure at the outlet.

This Figure confirms that the model correctly simulates single-phase flow (Darcy's law). The red and yellow regions represent areas of high pressure, while the blue regions correspond to low pressure. The color transition suggests that the pressure drop is continuous.

This result validates that the porous network effectively transmits the applied pressure with agreement with (Hannaoui et al., 2015)

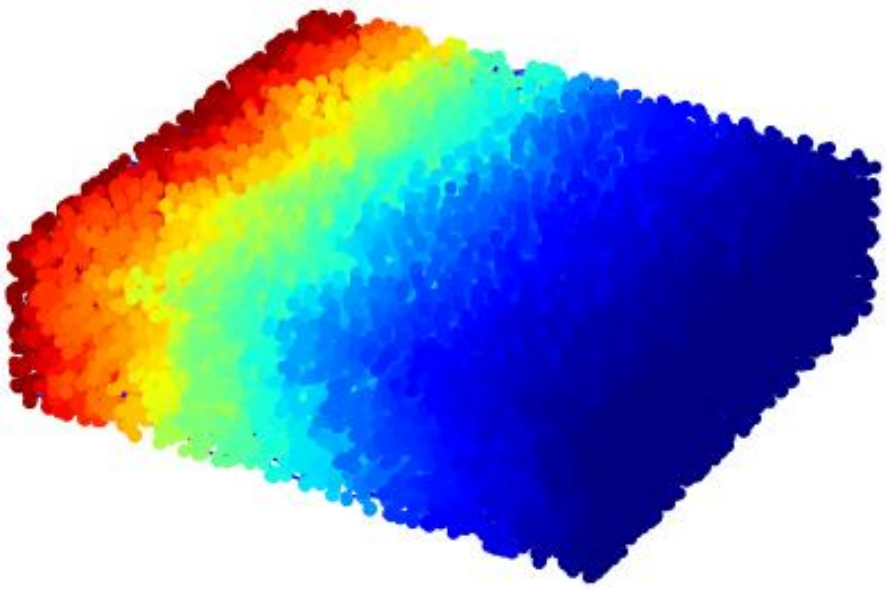

Figure 17: pressure drop inside the network

The results in Table 6 reveal a significant variation in permeability depending on the geometric model: cubes and cuboids exhibit the highest permeability, whereas trapezoids and rectangles show the lowest value. This trend is consistent with studies on pore networks, which demonstrate that permeability primarily depends on the size, shape, and connectivity of pores and throats (Yang et al., 2020) . Models with wider pores and more direct connections, such as cuboids, facilitate fluid transport and thus provide higher transmissivity and maximize permeability, whereas elongated, irregular, or poorly connected pores reduce it.

3.2.2. Predicting tortuosity in PNM

Tortuosity is a measure of the complexity or sinuosity of paths within a porous medium, describing how much the actual flow paths deviate from a straight line between two points. The classical definition is the actual length divided by the direct length. In reality, there are many actual pathways that matter could move through. This means that the actual length should more precisely be thought of as the average path length.

$$\tau = \left(\frac{L_{actual}}{L_{direct}}\right)^2 \qquad (3.\ 3)$$

But tortuosity is most easily determined as a fitting factor to transport data. We can use the effective diffusivity measured from the Fickian diffusion simulation and the known diffusivity of air to solve for the tortuosity.

$$\tau = \mathcal{E}\frac{D_{AB}}{D_{eff}} \qquad (3.\ 4)$$

Where $\mathcal{E}$ is the porosity, D_{AB} the known diffusivity of air and D_{eff}, the effective diffusivity due to the tortuous paths.

The effective diffusivity of the network is determine by solving Fick's law as shown below.

$$D_{eff} = \frac{N_A L}{A\Delta C} \qquad (3.\ 5)$$

With N_A the molar flow rate and ΔC the concentration gradient driving diffusion

After the concentration diffusion on Figure 19(c), PNM yielded a tortuosity of 1.41.

3.3. CFD Simulation

In this work, the CFD library OpenFOAM® is used to simulate a single-phase flow through porous electrodes in order to obtain the representative flow properties of these structures, including tortuosity and saturated permeability. High-resolution micro-computed tomography (micro-CT) image stacks of the porous electrodes serve as the basis for reconstructing the pore-scale geometry using *Fiji*. The resulting three-dimensional digital reconstructions are cropped into smaller, representative volume elements of about $250 \times 250 \times 250$ pixels and subsequently meshed with the *snappyHexMesh* utility. One exemplary computational mesh is shown in Figure 18. Towards the solid walls the mesh is refined to catch the correct geometry in the snapping step of the algorithm.

After generating the mesh, consisting of approximately 3 million cells, the Navier–Stokes equations described in Section 2.2.1 are solved. The applied boundary conditions are as follows: a defined pressure drop is imposed by prescribing constant pressures at the inlet and outlet, a no-slip (zero velocity) condition is applied at the pore walls, and symmetry conditions are imposed along the lateral boundaries. In this way, the simulations were performed for the smaller samples of the porous electrode.

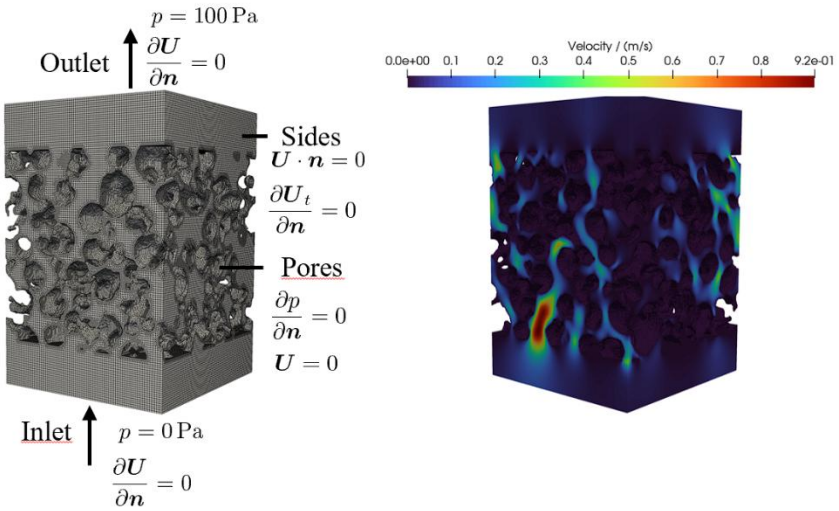

Figure 18: Computational mesh (left) with the patch names and an exemplary velocity distribution (right

After each simulation, the resulting volumetric flow rates through the samples were used to calculate the saturated permeability according to Equation 3.7. The tortuosity in each direction of the porous electrode was then determined; for example, the x-component is e.g. calculated as

$$\tau = \frac{\langle |\boldsymbol{u}| \rangle}{\langle u_x \rangle} \qquad (3.\ 6)$$

using the spatial average $\langle |\mathbf{u}| \rangle$ of the absolute local flow velocity and the velocity component in flow direction u_x. Afterwards, the arithmetic average of the results for the permeability and tortuosities are taken which represent the properties of the porous electrode.

3.4. Comparison of PNM and CFD for single phase flow

Both PNM and CFD simulations were performed on the identical pore structures, the sintered Nickel derived from µCT data to model single-phase flow. The pressure and concentration fields from PNM and CFD showed smooth gradients from inlet to outlet, validating physical consistency as shown on Figures 17(a) and 17(b), pressure gradient PNM and CFD and Figure17(c) and 17(d) concentration gradient PNM and CFD, respectively.

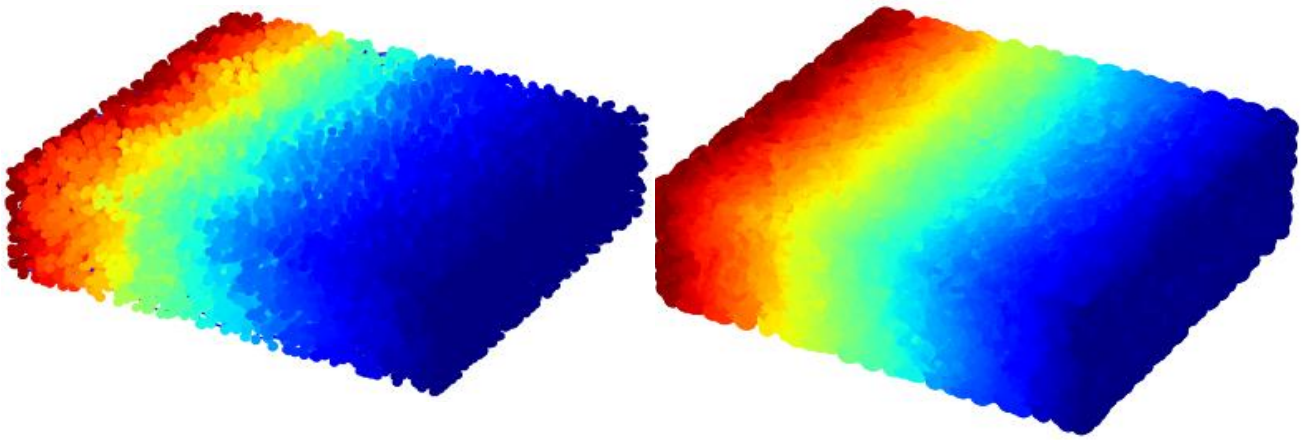

(a) (c)

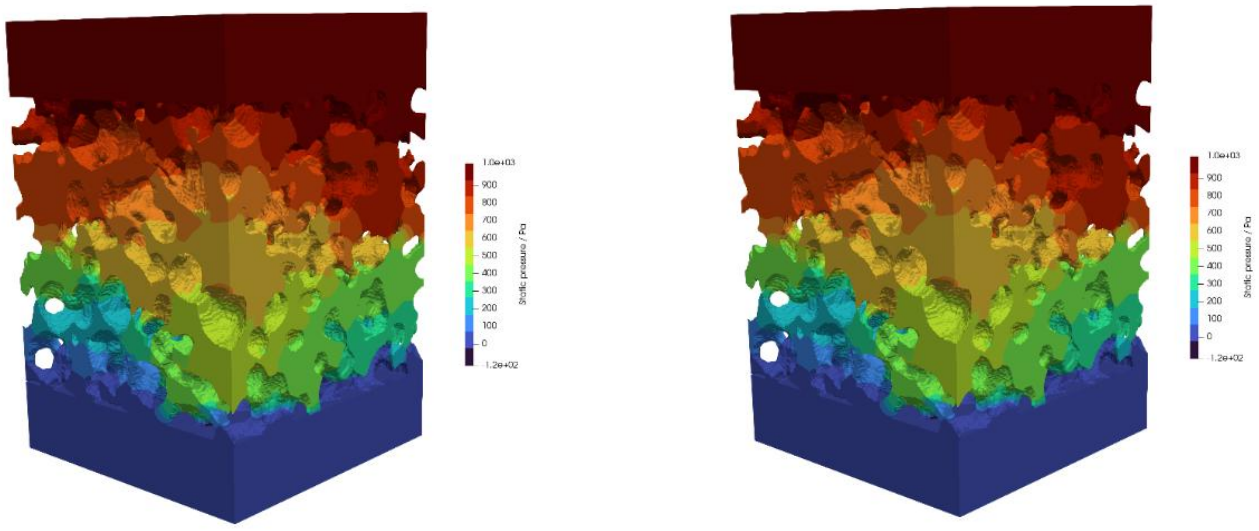

(b) (d)

Figure 19: Pressure profile PNM(a) CFD(b) and concentration profile for PNM(c) and CFD(d)

As discussed, red represents the inlet which has the highest concentration and pressure and the blue represents the outlet boundary with low pressure and concentration.

The tortuosity and the permeability of the porous electrode are shown in Table 7. Since the permeability depend on the geometrie of the pores and throats, the results from five different geometric models available in openPNM are included.

Table 7: Permeability and tortuosity comparison between CFD and PNM

	CFD	**PNM**		**Error (%) = |(K_PNM−K_CFD)|/K_CFD *100**
Permeability K(m²)	2.01e-12	Cones and cylinders	1.67e-12	
		Cubes and cuboids	7.247e-12	260
		Pyramids and cuboids	2.586e-12	28
		Squares and rectangles	8.823e-13	56
		Trapezoids and rectangles	3.791e-13	81
Tortuosity	1.39	1.41		1.4

The comparison of tortuosity between CFD and PNM shows good agreement, with less than 1.5% error. This excellent agreement illustrates PNM's capability in capturing the topological

complexity of transport pathways independent of the exact geometric assumptions of pore shapes. Such accuracy for tortuosity prediction aligns with literature acknowledging PNM's strength in representing connectivity and diffusion pathways in porous electrodes (Gostick, 2017; Huang et al., 2020).

Permeability results show variable agreement depending on pore and throat geometry, with relative errors ranging from 17% up to 260%.

For “Cones and cylinders” and “pyramids, and cuboids”’, PNM permeability is close to CFD with a error of 17% and 28% respectively. Other geometric models such as “cubes and cuboids” and “squares and rectangles”, produced much larger discrepancies, with errors up to 260%. This pronounced sensitivity arises because the hydraulic conductance of each conduit element a core parameter governing flow resistance, is directly linked to the assumed pore-throat shape, size, and connectivity. Inaccurate or oversimplified geometric models fail to capture the intrinsic morphological complexity of sintered nickel microstructures, leading to notable discrepancies. Therefore, it is critical to acknowledge that the predictive power of PNM for permeability cannot be taken as universally reliable without validation. Prior validation of the geometric model using CFD simulations or experimental data on representative samples is necessary before wider application. This step ensures that the chosen geometric accurately reflect the true pore network topology and hydraulic behavior.

This accurate simulation of tortuosity by PNM has important implications in electrolyser performance. The flexibility of PNM to simulate transport across diverse pore geometries efficiently as for permeability simulation, allows evaluation of multiple pore architectures.

This capability makes PNM especially suitable for optimizing porous layers in electrolysers, where:

Different porous architectures can be simulated and compared to identify those with the most efficient transport properties such as higher permeability and optimal tortuosity.

Designers can design microstructures for enhanced reactant supply and product removal performance, improving electrolyzer efficiency, durability, and operational stability.

The approach supports accelerated innovation by enabling assesssment of various microstructure candidates before costly and time-consuming experimental analysis or accurate CFD simulations.

3.5. Comparison of computational cost

In this study, the CFD simulations using OpenFOAM were performed on representative volume elements of the porous electrode microstructure with a mesh size around 250×250×250 voxels. Each of the 20 CFD simulations required approximately 20 minutes of computational time running on 8 CPU cores. By contrast, the PNM simulations, which included pore network extraction and single-phase flow simulations on the entire reconstructed microstructure, took approximately 15 minutes in total and were completed on a standard 1 core computer.

The result show that PNM is around 8 times faster than CFD, consistent with literature findings that emphasize PNM's computational efficiency for porous media simulations (Fathiganjehlou et al., 2023; Jung, 2020). This high difference in computational time clearly demonstrates the advantag**e** of PNM for rapid and large-scale simulations.

Conclusion

In this section, the results obtained from pore network extraction and transport simulations were presented, analyzed and discussed. The geometric properties derived from the extracted network showed strong agreement with direct image analysis, confirming the fidelity of the Snow2 reconstruction method. Simulations conducted with both PNM and CFD provided transport properties, permeability and tortuosity, with tortuosity values exhibiting particularly close alignment between the two methods, indicating that PNM reliably captures the complexity of diffusion paths. However, for permeability, the thesis details that the predicted values from PNM depend strongly on the choice of geometric model used for pore and throat representation in the network.

Conclusion

The main objective of this work was to perform a comparative analysis of pore network modeling (PNM) and computational fluid dynamics (CFD) approaches for transport modeling in porous materials, using real three-dimensional microstructures of sintered nickel obtained from X-ray microtomography (µCT).

To achieve this goal, the first step consisted of reconstructing pore networks from µCT images by applying the SNOW2 extraction method available in OpenPNM. The geometrical properties computed from these networks, such as porosity and interfacial surface area per volume, were then compared with available experimental data to validate the extraction method. This validation step is essential since geometrical properties strongly affect the accuracy of the subsequent transport simulations.

In the last step, transport simulations were carried out using both CFD and PNM approach, and the obtained results were compared. The aim of this comparison was to evaluate the accuracy of PNM approch.

In terms of permeability, PNM predictions proved to be highly dependent on the assumed pore and throat geometry. Among the tested models, “cones and cylinders” and “pyramids and cuboids” produced values that were consistent with CFD, with errors of 17% and 28% respectively. Conversely, other geometrical assumptions such as cubes, rectangles, or trapezoids resulted in very large discrepancies (ranging from 56% up to 260%), demonstrating that such geometrical idealizations are not suitable for describing this type of porous medium.

On the other hand, the tortuosity value obtained by PNM showed an excellent agreement with CFD, with only 1.4.% error. This confirms that the pore network modeling can faithfully capture the connectivity and transport pathways within the porous structure.

These findings show that, for the sintered nickel structures under study:

- PNM is a reliable and computationally efficient approach for evaluating tortuosity.

- For permeability, the predictive accuracy of PNM depends strongly on pore and throat geometric model. Therefore, prior validation on a small representative sample of the porous medium using CFD or experimental data is required to select the most appropriate geometry before applying PNM to the entire porous structure.

If such a validation step is conducted, PNM can be considered as an effective method for simulating transport properties in porous electrodes, and its speed and flexibility make it particularly suitable for parametric studies and microstructure optimization.

Future work will focus on confirming the accuracy of PNM in multiphase simulations to extend its applicability to complex transport phenomena in porous materials.

Bibliographic references

1. Böhme, Gert (2000). *Strömungsmechanik nichtnewtonscher Fluide: mit 49 Aufgaben*. 2., völlig neubearb. und erw. Aufl. Leitfäden der angewandten Mathematik und Mechanik 52. OCLC:248696788. Stuttgart: Teubner. 352 pp.
2. Davey, Reginald. (2025, January 17). The Different Types of Hydrogen: An Overview. AZoCleantech. Retrieved on September 16, 2025 from https://www.azocleantech.com/article.aspx?ArticleID=1894.
3. De Sá, Maria Helena (Mar. 2024). "Electrochemical Devices to Power a Sustainable Energy Transition—An Overview of Green Hydrogen Contribution". en. In: *Applied Sciences* 14.5, p. 2168. issn: 2076-3417. doi: 10.3390/app14052168. url: https://www.mdpi.com/2076-3417/14/5/2168 (visited on 06/20/2025).
4. Eghbalmanesh, A., Fathiganjehlou, A., Rieder, D. R., Hoogendoorn, M., Miloshevska, M., Baltussen, M. W., Peters, E. A. J. F., Buist, K. A., & Kuipers, J. A. M. (2024). CFD-validated pore network modeling of packed beds of non-spherical particle. *Chemical Engineering Science, 283*.
5. Emam, Abdelrahman S. et al. (Apr. 2024). "A review on recent trends, challenges, and innovations in alkaline water electrolysis". en. In: *International Journal of Hydrogen Energy* 64, pp. 599–625.
6. Fathiganjehlou, A., Eghbalmanesh, A., Baltussen, M. W., Peters, E. A. J. F., Buist, K. A., & Kuipers, J. A. M. (2023). Pore network modelling of slender packed bed reactors. *Chemical Engineering Science, 273*.
7. Ferziger, J.H. and Peric, M. (2002) Computational Methods for Fluid Dynamics. 3rd Edition, Springer,
8. Gackiewicz, Bartłomiej et al. (Mar. 2021). "An intercomparison of the pore network to the Navier–Stokes modeling approach applied for saturated conductivity estimation from X-ray CT images". en. In: *Scientific Reports* 11.1, p. 5859. issn: 2045-2322. doi: 10.1038/s41598-021-85325-z. url: https://www.nature.com/articles/s41598-021-85325-z (visited on 05/19/2025).

9. Gostick, Jeff et al. (July 2016a). “OpenPNM: A Pore Network Modeling Package”. In: *Computing in Science & Engineering* 18.4. Publisher: Institute of Electrical and Electronics Engineers (IEEE), pp. 60–74.
10. Gostick, Jeff T. (Aug. 2017). “Versatile and efficient pore network extraction method using marker-based watershed segmentation”. en. In: *Physical Review E* 96.2, p. 023307. issn: 2470-0045, 2470-0053. doi: 10.1103/PhysRevE.96.023307. url: https://link.aps.org/doi/10.1103/PhysRevE.96.023307 (visited on 06/25/2025).
11. Hannaoui, R. et al. (Feb. 2015). “Pore-network modeling of trickle bed reactors: Pressure drop analysis”. en. In: Chemical Engineering Journal 262, pp. 334–343.
12. Huang, Xiang, Wei Zhou, and Daxiang Deng (Nov. 2020). “Validation of pore network modeling for determination of two-phase transport in fibrous porous media”. en. In: *Scientific Reports* 10.1. Publisher: Springer Science and Business Media LLC. issn: 2045-2322. doi: 10.1038/ s41598-020-74581-0. url: https://www.nature.com/articles/s41598-020-74581-0 (visited on 07/11/2025).
13. Jung, Seongyeop (2020). Estimation of relative transport properties of fuel cell and electrolyzer transport layers by pore network and continuum based direct simulations, master,151 pages.
14. Khan, Zohaib Atiq, Ali Elkamel, and Jeff T Gostick (Nov. 2020). “Efficient extraction of pore networks from massive tomograms via geometric domain decomposition”. en. In: *Advances in Water Resources* 145, p. 103734. issn: 03091708. doi: 10.1016/j.advwatres.2020.103734.
15. Li, Guang-yao et al. (Feb. 2021). “Effects of particle gradation and geometry on the pore characteristics and water retention curves of granular soils: a combined DEM and PNM investigation”. en. In: *Granular Matter* 23.1, p. 9. issn: 1434-5021, 1434-7636. doi: 10.1007/s10035-020-01063-5. url: http://link.springer.com/10.1007/s10035-020-01063-5 (visited on 06/26/2025).
16. Misaghian, N. (2022). Multiphysics pore network simulation of electrochemical devices as a design tool, thesis, University of Waterloo, Canada, 171 pages.
17. Moukalled, F.; Mangani, L.; Darwish, M. *The Finite Volume Method in Computational Fluid Dynamics: An Advanced Introduction with OpenFOAM® and Matlab*; Fluid Mechanics and Its Applications; Springer International Publishing: Cham, 2016; Vol. 113. https://doi.org/10.1007/978-3-319-16874-6.

18. Rezaee, M R, A Jafari, and E Kazemzadeh (Dec. 2006). “Relationships between permeability, porosity and pore throat size in carbonate rocks using regression analysis and neural networks”. en. In: *Journal of Geophysics and Engineering* 3.4, pp. 370–376. issn: 1742-2132, 1742-2140. doi: 10.1088/1742-2132/3/4/008. url: https://academic.oup.com/jge/ article/3/4/370-376/5127671 (visited on 09/03/2025).
19. Riaz, Muhammad Adil et al. (2025). “Water electrolysis technologies: the importance of new cell designs and fundamental modelling to guide industrial-scale development”. en. In: *Energy & Environmental Science* 18.11, pp. 5190–5214. issn: 1754-5692, 1754-5706. doi: 10.1039/D4EE05559D. url: https://xlink.rsc.org/?DOI=D4EE05559D (visited on 07/31/2025).
20. Russo, A. (2024). Porous electrodes for water alkaline electrolysis. Technical University of Denmark 151 pages.
21. Sadeghi, Mohammad Amin et al. (2019). “Exploring the Impact of Electrode Microstructure on Redox Flow Battery Performance Using a Multiphysics Pore Network Model”. en. In: *Journal of The Electrochemical Society* 166.10, A2121–A2130. issn: 0013-4651, 1945-7111. doi: 10.1149/2.0721910jes. url: https://iopscience.iop.org/article/10.1149/2. 0721910jes (visited on 06/24/2025).
22. Sebbahi, Seddiq et al. (Sept. 2024). “A comprehensive review of recent advances in alkaline water electrolysis for hydrogen production”. en. In: *International Journal of Hydrogen Energy* 82, pp. 583–599. issn: 03603199. doi: 10.1016/j.ijhydene.2024.07.428. url: https:
23. //linkinghub.elsevier.com/retrieve/pii/S0360319924031161 (visited on 07/31/2025).
24. Sheng, Qiang (Mar. 2013). “Pore-to-continuum Multiscale Modeling of Two-phase Flow in Porous Media”. en. Doctor of Philosophy. Louisiana State University, Agricultural, and Mechanical College. doi: 10.31390/gradschool_dissertations.3790. url: https:// repository.lsu.edu/gradschool_dissertations/3790 (visited on 06/26/2025).
25. Vidas, Leonardo and Rui Castro (Dec. 2021). “Recent Developments on Hydrogen Production Technologies: State-of-the-Art Review with a Focus on Green-Electrolysis”. en. In: *Applied Sciences* 11.23, p. 11363. issn: 2076-3417. doi: 10.3390/app112311363. url: https://www. mdpi.com/2076-3417/11/23/11363 (visited on 07/31/2025).
26. Wang, C., Wu, K., Scott, G. G., Akisanya, A. R., Gan, Q., & Zhou, Y. (2020). A New Method for Pore Structure Quantification and Pore Network Extraction from SEM Images. *Energy &*

Fuels, *34*(1), 82–94. https://doi.org/10.1021/acs.energyfuels.9b02522

27. Wu, Yutong et al. (Feb. 2025). “Research progress of the porous membranes in alkaline water electrolysis for green hydrogen production”. en. In: *Chemical Engineering Journal* 505, p. 159291. issn: 13858947. doi: 10.1016/j.cej.2025.159291. url: https://linkinghub. elsevier.com/retrieve/pii/S1385894725000907 (visited on 08/02/2025).
28. Yang, Feichen et al. (July 2020). “Alkaline Water Electrolysis at 25 A cm^2 with a Microfibrous Flow-through Electrode”. en. In: *Advanced Energy Materials* 10.25, p. 2001174. issn: 16146832, 1614-6840. doi: 10.1002/aenm.202001174. url: https://onlinelibrary.wiley. com/doi/10.1002/aenm.202001174 (visited on 08/02/2025).
29. Yi, Zhixing et al. (Apr. 2017). “Pore network extraction from pore space images of various porous media systems”. en. In: *Water Resources Research* 53.4, pp. 3424–3445. issn: 00431397, 1944-7973. doi: 10.1002/2016WR019272. url: https://agupubs.onlinelibrary. wiley.com/doi/10.1002/2016WR019272 (visited on 06/26/2025).